

# Fabrication, microstructure and micromechanical properties of Fe-based metallic glass coating manufactured by laser

Peilei Zhang<sup>a,b,c\*</sup>, Qi Zhang<sup>a,b</sup>, Hua Yan<sup>a,b</sup>, Zhishui Yu<sup>a,b\*</sup>, Jin Yang<sup>a,b</sup>, Jieshi Chen<sup>a,b</sup>, Di Wu<sup>a,b</sup>, Haichuan Shi<sup>a,b</sup>,  
Yingtao Tian<sup>d</sup>, Songyun Ma<sup>e</sup>, Weisheng Lei<sup>a,b</sup>

<sup>a</sup> School of Materials Engineering, Shanghai University of Engineering Science, Shanghai 201620, China

<sup>b</sup> Shanghai Collaborative Innovation Center of Laser Advanced Manufacturing Technology, Shanghai 201620, China

<sup>c</sup> Fraunhofer Institute for Laser Technology ILT, Aachen 52074, Germany

<sup>d</sup> Department of Engineering, Lancaster University, Lancaster LA1 4YW, United Kingdom

<sup>e</sup> Institute of General Mechanics, RWTH Aachen University, Aachen 52062, Germany

## Abstract

Iron-based amorphous alloys have received extensive attention due to their high hardness, elastic modulus/limit and wear/corrosion resistance. In this research, an attempt has been made to develop an amorphous coating of Fe-Cr-Mo-C-B-Y metallic glass coating on the steel substrate through laser surface treatment. During the test, various process parameters are used to determine the position of the amorphous phase. After coating, the microstructure and phase distribution of the coating were analyzed by scanning electron microscope, X-ray diffraction and transmission electron microscope. Mechanical properties of the coating were analyzed by using microhardness testing, abrasion resistance and nanoindentation methods. The results show that the coating thickness varies directly with the incident laser power and interaction time. The microstructure of the coating can be divided into three layers: the first layer (columnar crystals), the second layer (the crystalline phase filled with the unit structure) and the third layer (the unit structure consists of a crystalline phase and an amorphous phase). As the heat input of laser cladding decreases, the volume fraction of the amorphous phase increases, and the average microhardness and nanohardness increase.

**Keywords:** Laser cladding; Amorphous coating; Composite coating; Metallic glass; Nanoindentation;

## 1. Introduction

As an important surface modification method laser cladding is widely used due to its characteristics great heat

---

\* Corresponding authors: peilei@sues.edu.cn (Peilei Zhang) and yu\_zhishui@163.com (Zhishui Yu)

input and shorter cooling time can be released by high power lasers [1]. These characteristics makes grain refinement hardness has been improved and connection between the coating and substrate achieve the combination of atoms [2–4]. The dilution ratio between the coating and the substrate after laser cladding is extremely low [5]. Laser cladding has been developed as an alternative to the existing casting processes [6]. Compared with the traditional surface treatment technologies such as surfacing, electroplating, vapor deposition, laser cladding has the advantages of low dilution, dense tissue coating. And substrate can form better metallurgical bonding, which is suitable for cladding material with many changes in grain size and content large and other characteristics [7,8]. In recent years, laser cladding as a new technology is applied to the surface modification of materials, such as gas turbine blades, gears [9]. On the other hand, laser cladding can also be used for surface repair products such as rotors, dies and so on [10]. Laser cladding is divided into prefabricated powder laser cladding, synchronized feeding laser cladding and wire laser cladding simultaneously [11]. In which the synchronized feeding type laser cladding technology is the most widely used [12]. In the cladding process the liquid pool is formed by the substrate and the metal powder sprayed by the powder feeding nozzle driven to be formed by laser irradiation. A great cooling rate can be obtained.

With the high yield and fracture strength, excellent wear resistance and relatively low cost, Fe-based bulk metallic glasses (BMGs) have attracted much attention [13,14]. However, these alloys find limited application as bulk structural material due to their extremely poor tensile ductility and toughness and restricted size/thickness to which they can be directly cast or fabricated [15]. On the other hand, bulk metallic glass can be a good candidate for wear/corrosion resistant coating on metallic components [16]. Therefore, it has proved to be feasible to form a protective layer containing amorphous on the surface of the member by means of laser cladding [17]. As a popular coating material, amorphous alloys coatings have been prepared on many materials [18]. However, when an amorphous coating is prepared by a laser cladding method, defects are present in the layer due to differences in physical properties between the coating and the material [19]. Wong tried to use Al–Si amorphous coating for a structural application by combining plasma-spray and laser melting [20]. Zhang [21] and Shu [22] used the laser cladding method to prepare the amorphous coating on the steel surface. Aghasibeig made to develop an amorphous coating with  $\text{Fe}_{8.1}\text{Cr}_{6.4}\text{Mn}_{5.3}\text{Si}_{6.9}\text{Mo}_{3.6}\text{C}$  alloy on AISI 1018 steel substrates using a diode laser [23]. Despite the wide range of experimental process parameters, after laser surface coating, the complete amorphous surface microstructure cannot be retained. However, continued studies on amorphous coating for structural application are warranted as significant success in retaining amorphous coating and obtaining high wear resistance has not yet been achieved [24]. Zhang have did many studies on Fe-based amorphous coatings by laser cladding method

[14,19,24–27]. A new Fe-based metallic glasses system suitable for laser process was developed and the compositions were redesigned according to the metallic glass rules proposed by Inoue [19,28]. Microstructure evolution, crystallization behavior, wear resistance, micromechanical properties and effect of special elements on glass form ability (GFA) of coating were studied in details [26]. For Fe-based amorphous coatings with laser process, the most important thing is to get a suitable microstructure for obtaining excellent properties [29]. In other words, getting a whole metallic glass structure in coating is not so critical to engineering in clad coatings [30]. Because sometimes a composite coating with nanocrystalline and amorphous phase has excellent friction performance under actual working conditions [31]. On the other hand, so far, cracks problem in laser amorphousing Fe-based coating has not been effectively solved [24]. Inherent brittle fracture characteristics for BMGs are difficult for laser preparation amorphous coating [32]. A soft phase introduced into the coating to improve the crack sensibility in rapid heat and cooling process with laser scanning [33]. This idea is also used in selective laser melting (SLM) Fe-based BMGs parts [34].

SLM is an important branch of 3D printing technology [35]. SLM scans the metal powder bed layer by layer according to the path planned in the 3D CAD slice model [36]. The scanned metal powder melts and solidifies to achieve the effect of metallurgical bonding, and finally obtains the metal parts designed by the model [37]. Recently, many researchers have attempted to produce BMGs using SLM method. A Swedish company, Exmet AB, was the first group to demonstrate the feasibility of this technique in 2011 [38,39]. In these two patents, method of producing BMGs by SLM was provided. SLM fabrication of BMGs started in 2013 by Simon Pauly according to the published literature [40]. With the new SLM technology, it can effectively break through the size limit, so that the three-dimensional size of the amorphous alloy can be designed and prepared according to the requirements of use. This has opened a new window for the promotion of the application of amorphous alloys in various industrial fields.

As an engineering coating with excellent performance, the importance of amorphous alloy coating is self-evident. A whole glassy microstructure obtained in the coating is no doubt good for the application of BMG coating by laser. But from another point of view, a composite coating containing amorphous and specific crystalline phases is not necessarily a bad thing for the overall performance of the coating itself. Therefore, how to design the microstructure and phase composition of the amorphous coating is the most important work. For a certain Fe-based amorphous alloy, controlling the cooling rate in the laser process is the most important method to design the microstructure in the amorphous coating. In this study, microstructure and micromechanical properties of Fe-Cr-Mo-C-B-Y metallic glass coating manufactured by laser is studied and the coating with the highest cooling

rate is obtained. The main goal of this work is to clarify the phase compositions, study the mechanical properties of each phase and explain the formation conditions of the amorphous phase in the coating with different cooling rates processed by laser.

## 2. Experimental procedure

The substrate used in this study was Q235 steel with dimensions of 50 mm × 50 mm × 10 mm. The surface of the substrate was washed with acetone and methanol to clean and degrease the surface. The amorphous alloy powder was produced by gas atomization technique with a particle size distribution of 53 - 150 μm. Table 1 shows the as-received chemical composition of the powder. The amorphous powder is mixed with the organic binder and coated on the surface of the substrate. The broad halo with diffused intensity can be seen in the XRD profile which is shown in Fig. 1 and it can be proved that the powder used has a very high amorphous content. A 5 kW high power continuous wave fiber laser was employed for laser processing metallic glasses coating on steel. The laser wavelength is 1070nm, and the laser spot size is 3.3 mm \* 2 mm rectangle.

Table 1 Chemical composition of the amorphous alloy powder (wt. %).

Element	Cr	Mo	C	Y	B	Fe
wt.%	14.32-15.02	25.10-26.2	3.24-3.75	3.10-3.60	1.10-1.42	Bal.

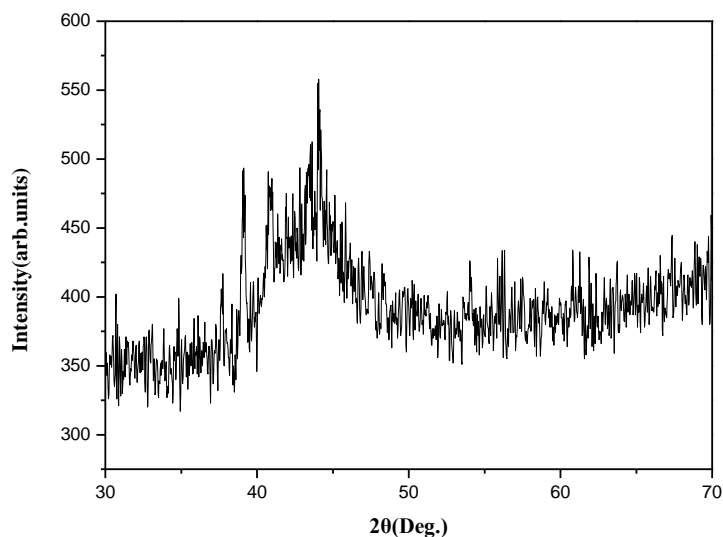


Fig 1 XRD pattern of the powder.

Microstructures and phase identifications were studied by X-ray diffraction (XRD) analysis using Cu K $\alpha$  radiation, scanning electron microscopy (SEM) and scanning transmission electron microscopy (STEM). XRD research mainly focuses on the main phase composition of laser coatings, and the residual stress was measured by

nanindentation. The sample was produced by grinding on 400, 800, and 1200 grit SiC pad and polishing with diamond paste on a micro cloth for microstructural studies by scanning electron microscope (SEM). In order to observe a clear microstructure under microscope and analyze the sample was etched with aqua-regia. The microhardness was carried out by microhardness test with a load of 0.5 N and loading time of 10 s. Tribological behavior of the coatings and substrate were evaluated using the rotating wear machine RETC MFT-5000 and analysis of microstructure of the worn surface by SEM.

For the content of amorphous phase, the effect of cooling rate is the key factor. Therefore, the Rosenthal formula was used to calculate the cooling rate during laser cladding under the action of a moving heat source [41].

$$\frac{\partial T}{\partial t} = 2\pi k \left[ \frac{v}{P} \right] (T - T_0)^2 \quad (1)$$

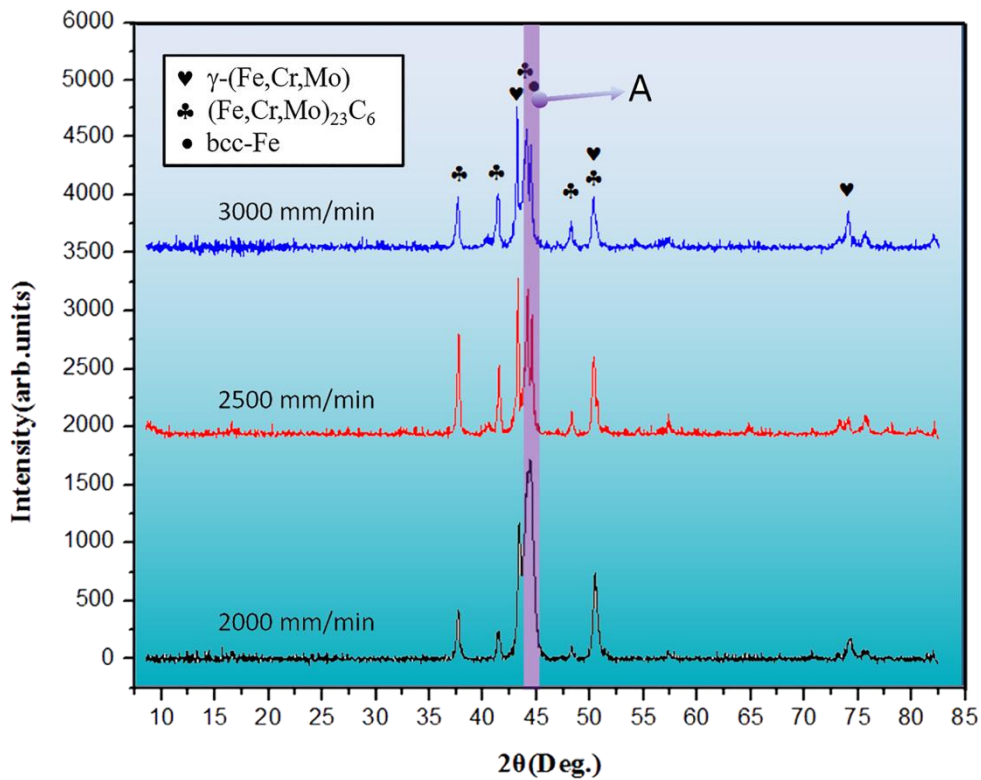
In this formula:  $k$  was the thermal conductivity,  $v$  was the scanning speed,  $P$  was the laser power, and  $T$  was the material initial temperature. It can be seen the cooling rate was equivalent to the reciprocal of the heat input in this formula. Therefore it can be concluded that the smaller heat input, the higher the cooling rate, and the more amorphous content in the layer can be obtained.

### 3. Results and discussion

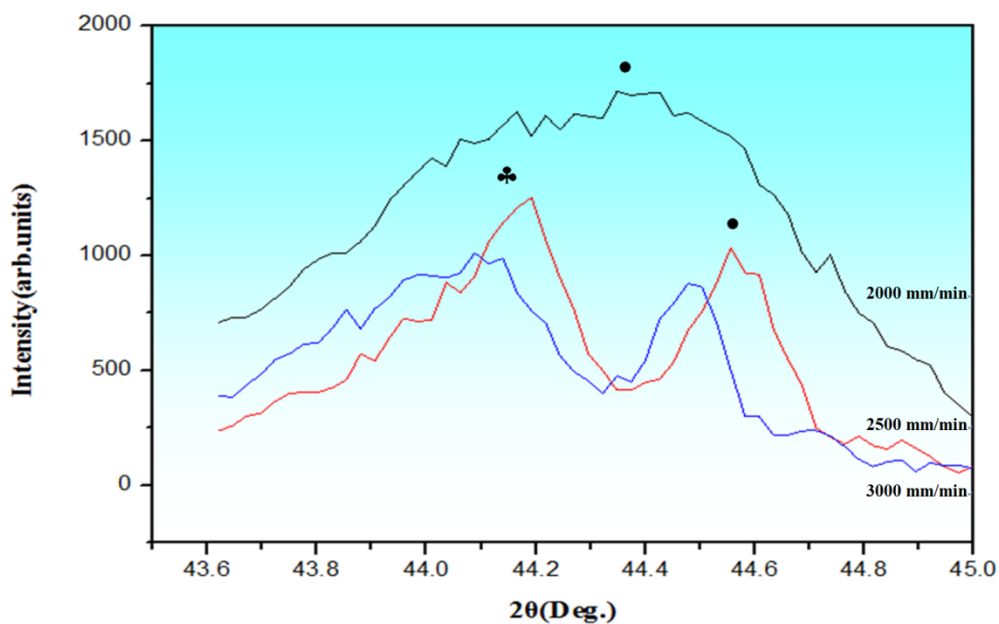
#### 3.1 XRD results of coatings

The XRD patterns of the cladding layers are shown in Fig. 2. Obviously, there were significant changes in XRD values of coatings with different scanning speed. But in the different coatings the phase constituents of the cladding coating were composed with  $M_{23}C_6$  ( $M=Fe, Cr, Mo$ ) and  $\gamma$ -( $Fe, Cr, Mo$ ) phases. This is mainly due to the fact that the samples detected by XRD were formed by overlapping multiple coating layers. Owing to the latter laser cladding coating would had an heat effect on the previous one. It can be seen easily that as the scanning speed increases, the peak value of XRD drops accordingly. It can be explained to a certain extent that as the scanning speed increases, the amorphous content in the coating is increasing. The wider diffraction peaks can be found when  $2\theta$  angle is about  $45^\circ$  and the peaks intensity which representing the content of  $\gamma$ -( $Fe, Cr, Mo$ ) and bcc-Fe phases decrease. The peaks of different coatings near  $45^\circ$  ( $2\theta$ ) were shown in the Fig. 2(b). As the cladding speed increases, the peak of the crystallization peak decreases and differentiates into two peaks from single bcc-Fe to bcc-Fe mixed with  $M_{23}C_6$ . Fig. 3 shows the XRD pattern in the center of the cladding coating, which the scanning speed was 3000 mm/s. Although there are still peaks that characterize the crystalline phase in the coating, the peaks are significantly reduced and the broadened diffraction peaks are more obvious than the slow scanning. The XRD curve shows that the amorphous phase content at the center of the coating is higher than that at the outermost

surface of the coating. The reason for this phenomenon is that the next laser scan will remelt the surface of the front layer coating and form a heat-affected zone on the subsurface layer, but the center of the coating is not greatly affected by this thermal effect, and the original amorphous structure can be maintained. status. X-ray diffraction results show that there is no bcc-Fe in this coating. The possible reason is that at fast scanning speed, some crystal phases are suppressed, and more alloys in the molten pool are retained in an amorphous state.



(a) Patterns of the coatings at different scan speed



(b) Patterns of the coatings at different scan speed when the  $2\theta$  is between  $43.6^\circ$  to  $45^\circ$  (Zone A in Fig.2 (a))

Fig 2 XRD patterns of the coatings at different scan speed

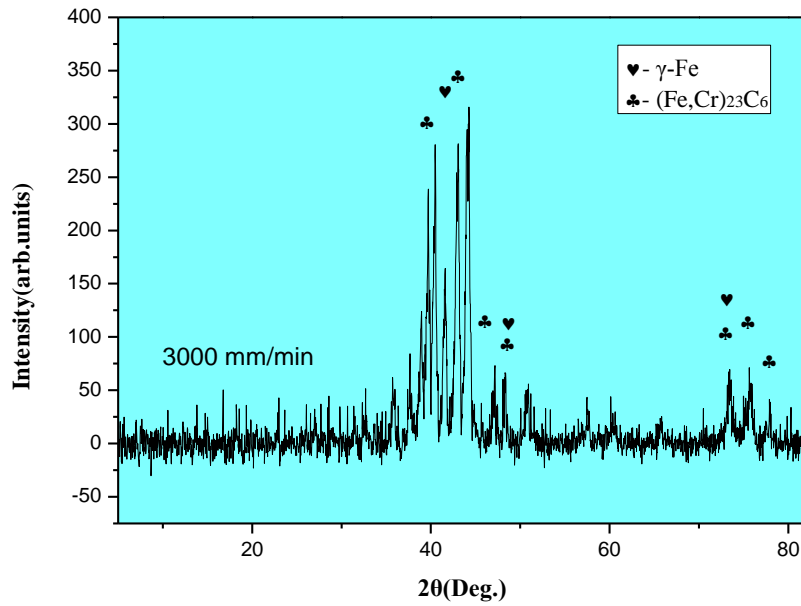


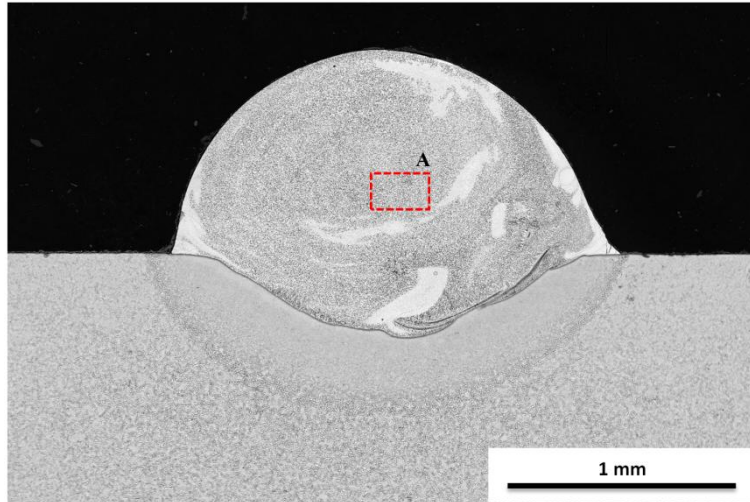
Fig 3 XRD patterns of coating in the center position

### 3.2 Microstructure characterization of coating

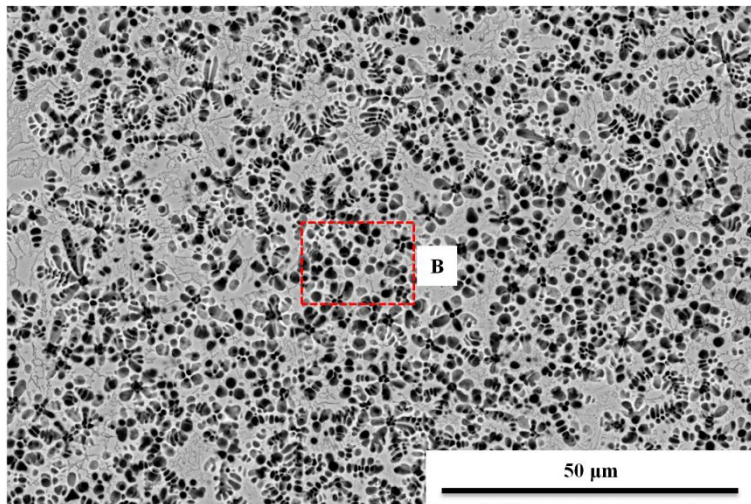
Table 2 shows the process parameters of laser cladding. The microstructure of the coating with different dilution rates is shown in Fig. 4. It can be seen that when the scanning speed is changed, the phase composition and dilution rate of different coatings are different. When the dilution rate is high, the coating is mainly composed of equiaxed crystals. As the dilution rate decreases, the phase composition changes, and the content of equiaxed crystals gradually decreases, becoming a unit structure composed of multiple different phases. Combined with the XRD results in Fig. 3, it can be further determined that the equiaxed crystal structure is bcc-Fe during low-speed scanning. The structure is mainly composed of white equiaxed crystals with black crystal phase in the middle and many white and gray precipitates on the edges. The amorphous phase is between the precipitated phase and the white phase [42]. The effect of scanning speed on this unit is shown in Fig. 5. As the cooling rate increases, the size of the cell becomes larger, which means that the content of the amorphous part increases. Therefore, as the laser scanning speed increases, the number of black phases and other crystalline phases decrease, and the content of amorphous phase increases. Moreover, coatings with more amorphous phase also have a better metallurgical bond with the substrate.

Table 2 Parameters of laser cladding process.

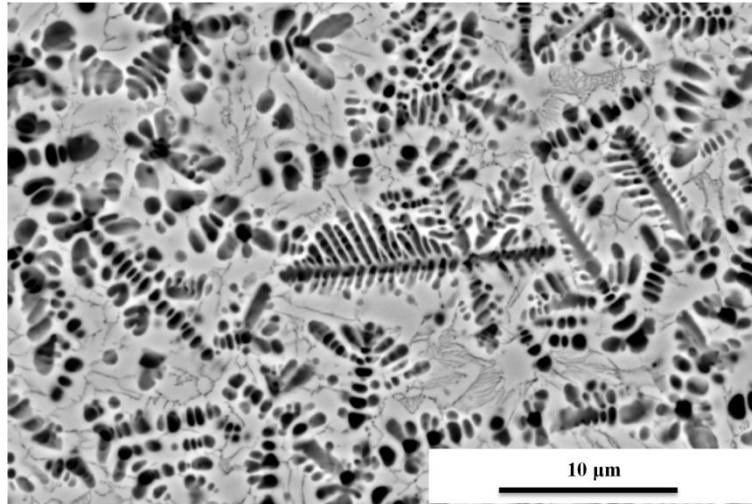
Defocus (mm)	Protective gas flow (L/min)	Laser power (W)	Scanning speed (mm/min)
45	15	4500	2000-3000



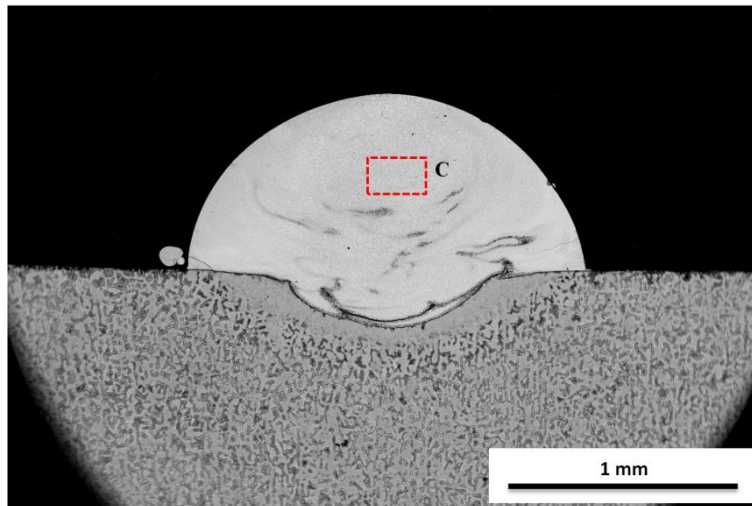
(a) Cross section of coating with high dilution rate



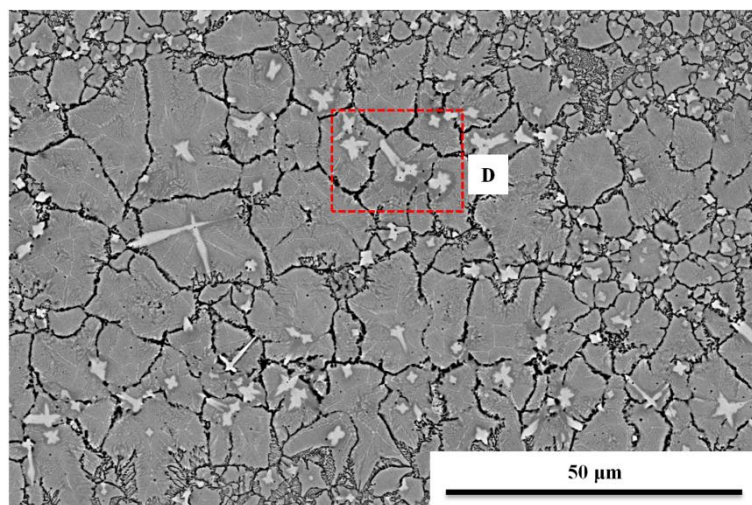
(b) The microstructure of area A in Figure 4(a)



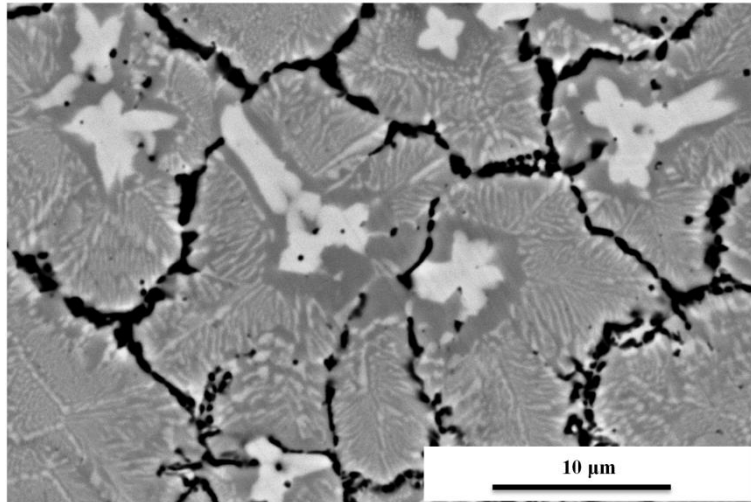
(c) The microstructure of area B in Figure 4(b)



(d) Cross section of coating with low dilution rate

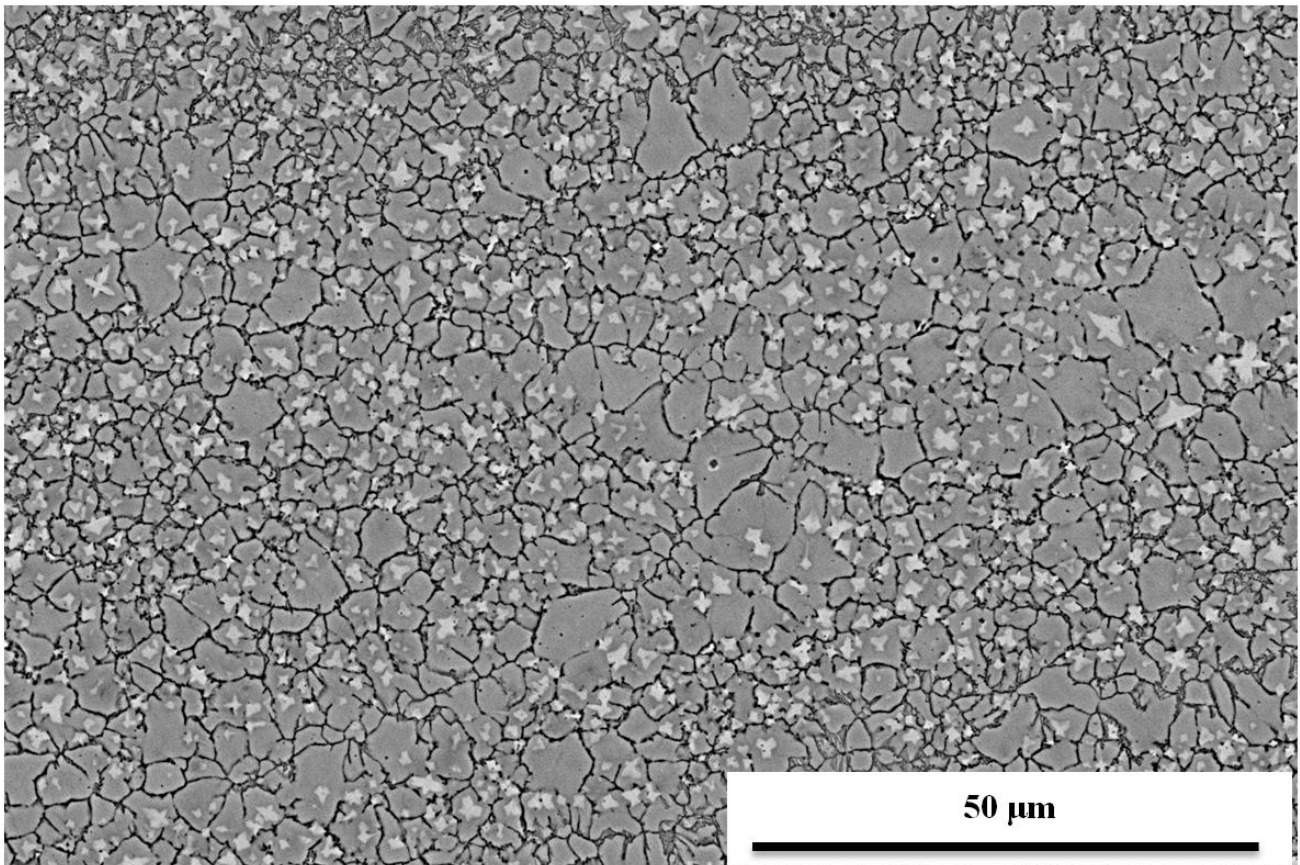


(e) The microstructure of area C in Figure 4(d)

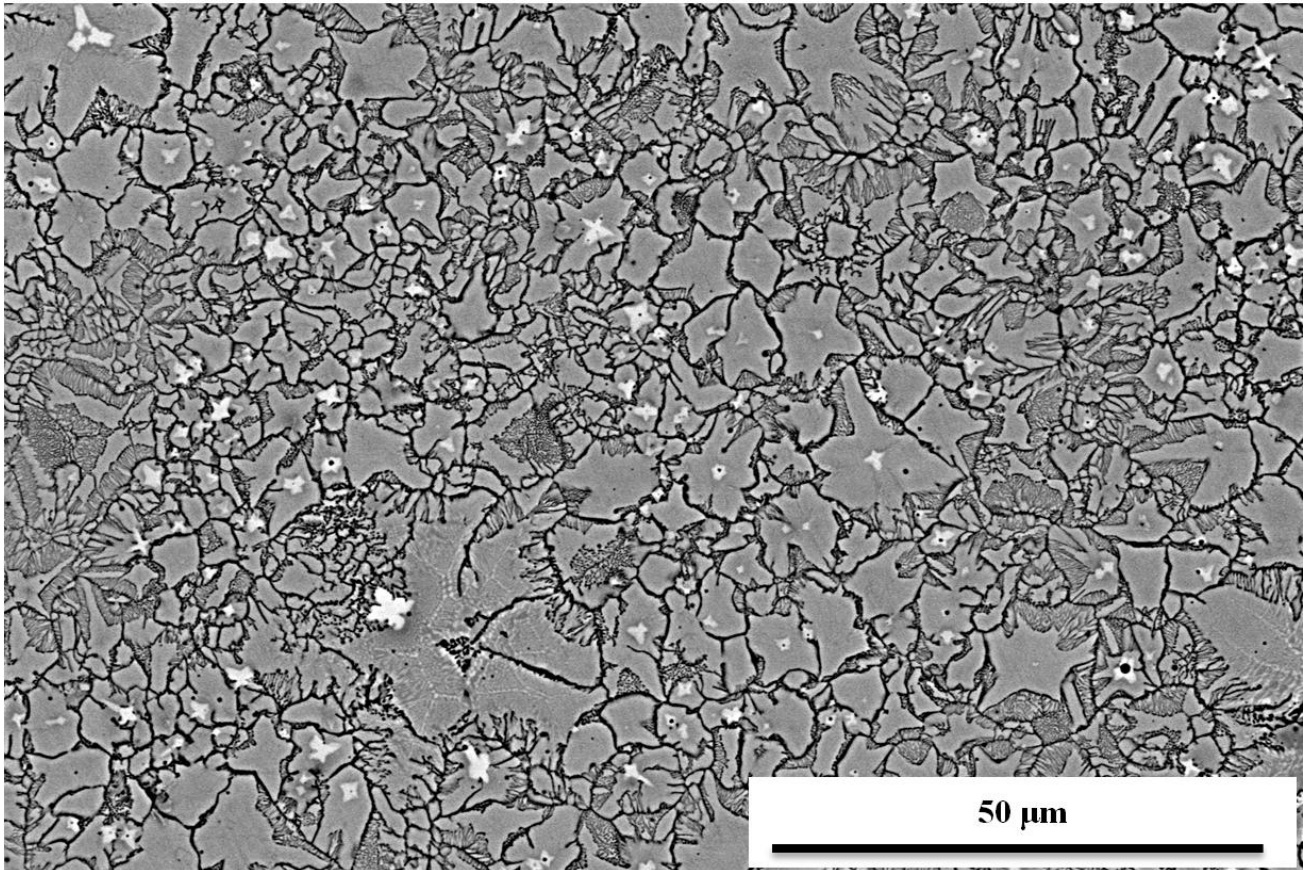


(f) The microstructure of area D in Figure 4(e)

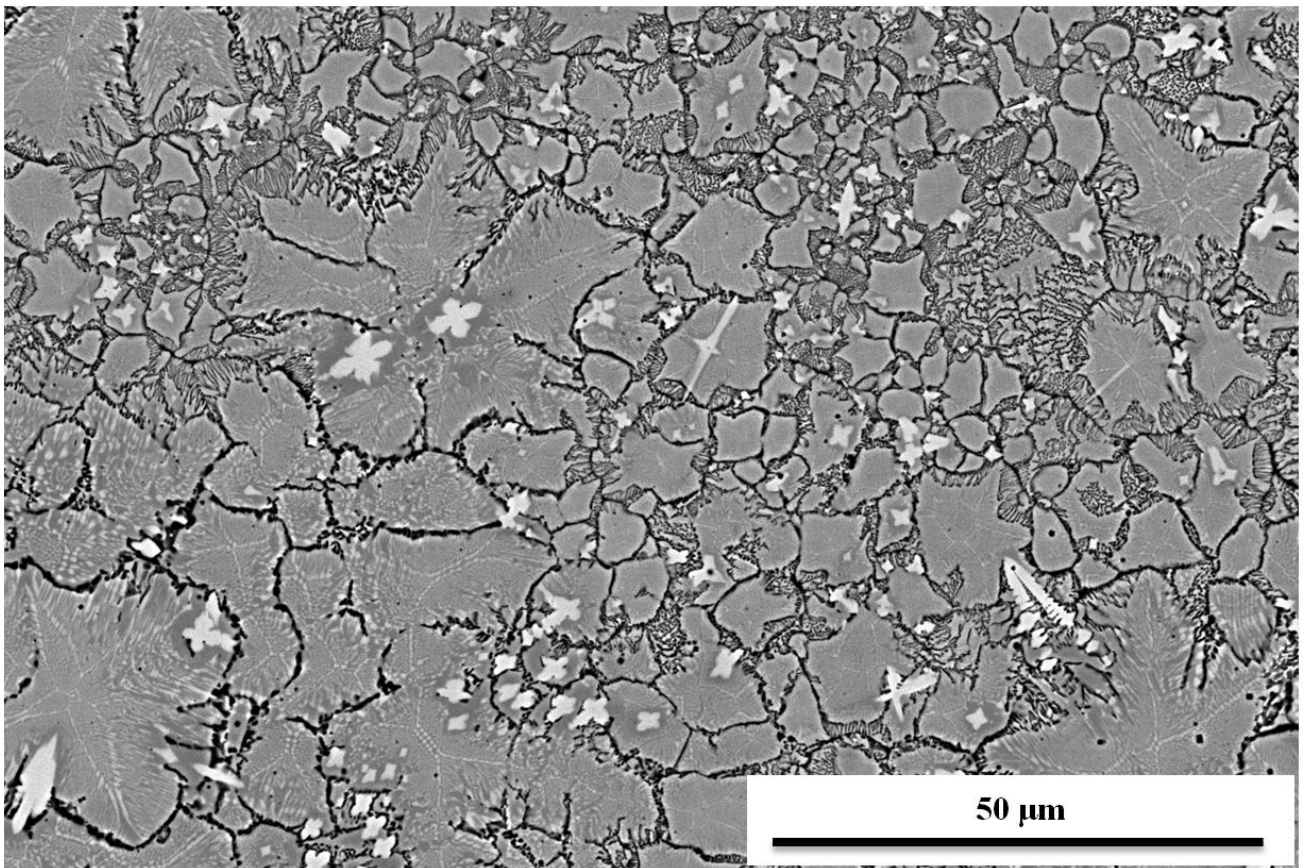
Fig. 4. SEM image of the coating with high and low dilution



(a) 2500 mm/min



(b) 2800 mm/min



(c) 3000 mm/min

Fig. 5 SEM image of the coating at different scanning speed

Although increasing the scanning speed can change the size of the unit structure and increase the amorphous content, the maximum speed within this range cannot guarantee that the coating has an absolutely high amorphous content. The amorphous content of this iron-based coating cannot reach the content similar to that of the zirconium-based amorphous coating [43]. The main reason is that the amorphous-forming ability of the iron-based amorphous alloy itself is weaker than that of the zirconium-based; secondly, the preset powder cladding due to the presence of the binder and the inability to flow, the cooling rate of the molten pool is lower than that of the simultaneous powder feeding cladding, but the way of presetting the powder is beneficial to the solidification and formation of the coating molten pool [44]. Fig. 6 shows the high-speed photography of the prefabricated powder laser cladding layer at different laser scanning speed. In the figure, the shape of the molten pool is described by a red curve. As the scanning speed increases, the size of the molten pool becomes longer, which means that the heat dissipation area of the molten pool increases, which is conducive to the cooling rate of the coating. However, the main structure of the coating has not changed significantly. Therefore, although the scanning speed is increased, the basic unit structure formed by the amorphous phase and the crystalline phase in the coating remains unchanged, and only the relative ratio of the amorphous phase to the crystalline phase changes. It should be noted that, compared with the coaxial powder feeding laser cladding process, the prefabricated powder laser cladding process has higher operability. However, due to the influence of heat dissipation conditions, the amorphous content of the preset powder coating did not increase significantly.

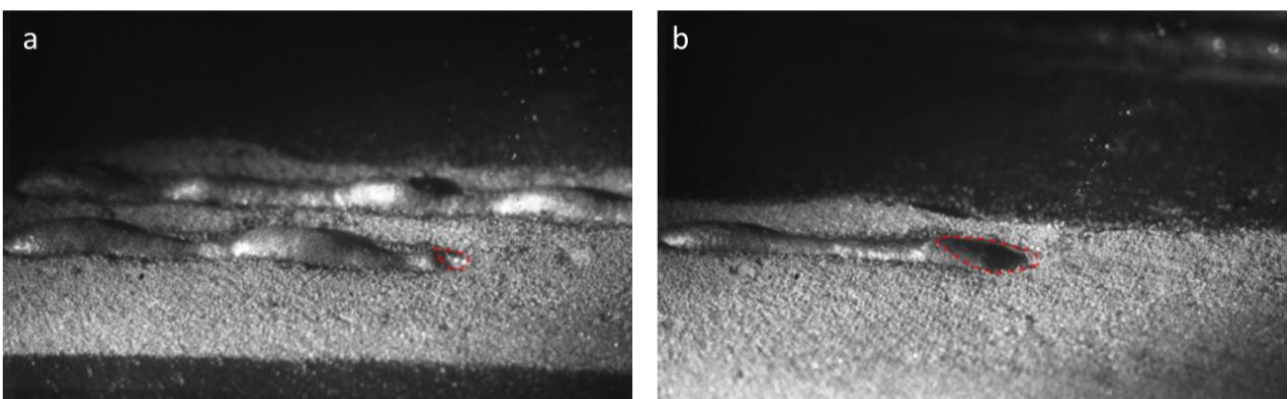


Fig. 6. High-speed photography of pre-made powder laser cladding a) 2000 mm/min; b) 3000 mm/min

Fig. 7(a) shows the macrostructure of the laser cladding coating with a smooth surface when the scanning speed is 3000mm/min, and no obvious cracks are observed on the coating surface. Fig. 7(b) shows a macro cross-sectional view of the coating. It can be clearly seen that the dilution rate of the coating to the substrate is

relatively small, and no cracks are found inside the coating. Because the cooling rate of different areas in the coating is different, the result is that the structure of each area is also different. Fig. 7(c) shows the top of the coating, with its unit structure filled with crystalline phases. During the cooling of the coating, the top area of the coating solidifies at the last moment, which provides sufficient growth time for the crystal phase in this area for large-area crystallization. Due to the dilution, in Fig. 7(d), the columnar crystals are grown from the base material by epitaxial growth and extended into the coating through competitive growth. The supercooling and the solute discharged from the tip of the columnar crystal into the solution prevent the growth of the columnar crystal [45]. It can be seen from Fig. 7(d) that the coating can be roughly divided into three layers: the first layer (columnar crystals), the second layer (the crystalline phase filled with the unit structure) and the third layer (the unit structure consists of the crystal phases and amorphous phase). And on different parts of the coating, the content of the amorphous phase is different. A schematic diagram of the different layers is shown in Fig. 7(e). The columnar crystals grown by epitaxial growth on the substrate can prove that the coating has a good metallurgical bonding ability with the base metal [46]. As the laser scanning speed increases, the columnar crystals in this area become smaller. The width of the second layer is about 8 - 10  $\mu\text{m}$ .

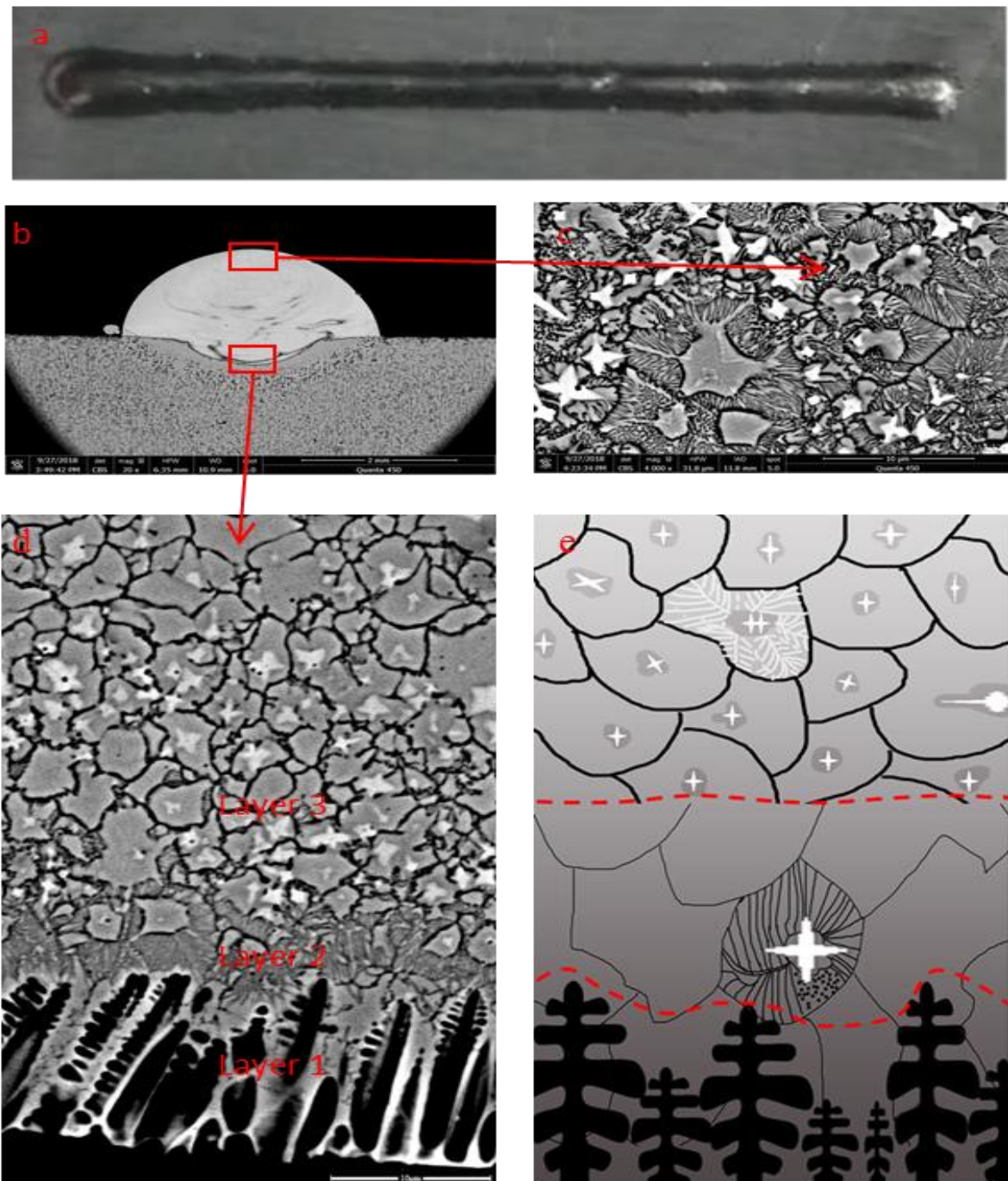


Fig. 7 (a) Macrostructure of the coating; (b) SEM image of the cross-section; (c) microstructure of the top of the coating; (d) microstructure of the intermediate of the coating (e) schematic illustration of the graded coating.

Because in the laser cladding process, the cooling rate decreases as the distance from the bottom of the molten pool increases [47]. There is a larger cooling rate in the first and second layers, but due to the dilution of the substrate, the alloy composition in these two places deviates from the original amorphous composition. According to the Gäumann's model, as columnar crystals grow, solutes will be repelled before the solidification interface [48]. This is the reason why a component supercooled area appears at the front end of the columnar crystal. In this area, nucleation occurs when the degree of subcooling is greater than the maximum growth degree of subcooling

required for nucleation [49]. However, in the third layer, due to the high degree of undercooling, the unit structure is filled with general crystal phases instead of fine equiaxed crystals. As the solid/liquid interface moves, a unit structure containing a mixed amorphous phase and a crystalline phase is formed, and the cooling rate of the third layer at the center easily reaches the critical cooling rate for forming the amorphous phase. Therefore, the formation of the amorphous phase requires not only a large cooling rate, but also a suitable alloy composition [50]. In the second layer, no equiaxed crystals similar to other amorphous coatings were found, but a unit structure based on the crystalline phase. This is mainly due to the strong mixing relationship in Fe-Cr-Mo amorphous alloys [51], but the main product  $M_{23}C_6$  has poor resistance to molybdenum [52]. Firstly, it precipitates in the melt due to the accumulation of molybdenum, and produces areas lacking molybdenum around, and increases the compositional supercooling of the melt. In this region, the amorphous melt has a very large viscosity, and the movement of molybdenum atoms is relatively difficult. As the cooling progresses, part of the amorphous state exists in the coating in a solidified state, but relatively small atoms can move and form grain boundaries at the last moment of cooling. Therefore, in the second layer, only unit structures based on crystal phases can be found. The microstructure of the third layer is shown in Fig. 8. Energy spectrum detection is performed at different positions in the unit structure. Table 3 shows the atomic percentage contents of elements in the white particle phase in the middle of the unit structure and the gray phase around the white particle phase. It can be seen that the content of molybdenum and iron varies greatly in different positions of the unit structure. The white phase was identified by energy ray analysis, and the result can be seen in Fig. 8(b). The results show that molybdenum is enriched in the white phase. During the solidification of the coating, the Mo-rich white phase grows out of the liquid metal in a heterogeneous nucleation manner, and discharges the solute element Fe to the surrounding liquid metal.

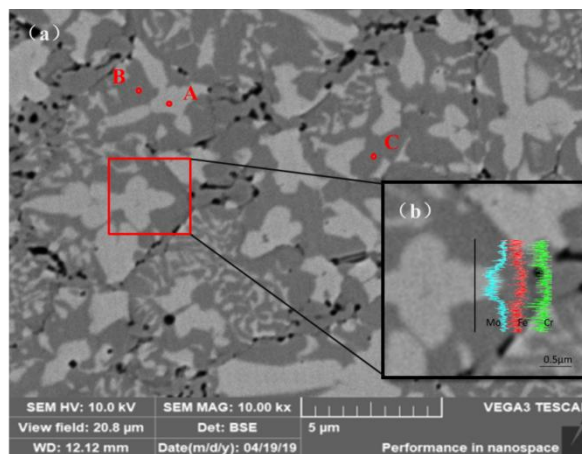


Fig. 8 scanning results of the coating (a)point (b) line

Table 3 EDS analyses results of test points in different region of coating

Points	Elements compositions (at. %)					
	Fe	Cr	Mo	C	Y	B
A	39.21	17.68	22.99	19.84	0.29	0.00
B	54.12	19.86	6.06	19.90	0.06	0.00
C	50.94	19.56	6.90	22.00	0.60	0.00

The result of the mapping scan of the coating is shown in Fig. 9. Combined with the XRD analysis results, the white primary phase in the coating is  $\gamma$ -(Fe, Cr, Mo). During the laser cladding process, excessive solid solution is caused by rapid solidification, and part of iron is replaced by molybdenum and chromium, resulting in a decrease in iron content in the molten pool. In the Fe-Cr-Mo-C-Y series amorphous alloy coatings, it is very common to calibrate the  $(\text{Fe, Cr})_{23}\text{C}_6$  phase, that is, to confirm the element types in the  $\text{M}_{23}\text{C}_6$  composite compound [51]. However, the appearance of molybdenum in this experiment proves that  $\text{M}_{23}\text{C}_6$  is not only a simple ternary mixture of iron, chromium and carbon. The presence of a small amount of molybdenum makes it possible for  $\text{M}_{23}\text{C}_6$  to exist as  $(\text{Cr, Fe})_{20}(\text{Cr, Fe, Mo})_3\text{C}_6$ .  $\text{M}_{23}\text{C}_6$  has a small amount of molybdenum dissolution in the second sublattice [51]. And through the energy spectrum analysis of the gray phase, the atomic ratio of element Fe, Cr, Mo and C is close to 4:1. This proves the existence of  $(\text{Cr, Fe})_{20}(\text{Cr, Fe, Mo})_3\text{C}_6$  in the coating.

The TEM image of Fe-Cr-Mo-C-Y-B laser cladding composite coating is shown in Fig. 10. Fig. 10(a) shows the TEM result of the mixed region of amorphous and  $\text{M}_{23}\text{C}_6$ . It can be clearly seen from the diffraction point that there is an amorphous state in the coating. The bright-field TEM image of the coating is shown in Fig. 10(c), and the selected area electron diffraction (SAED) results of the different regions are shown in Fig. 10(d) and Fig. 10(e). According to the SAED diagram, the gray and white needle-like phases in the unit structure are crystalline phases. Both crystalline phases have a face-centered cubic (FCC) structure. The atoms of Fe, Cr and Mo elements can be replaced with each other in the coating. Compared with the XRD pattern results, the  $\text{M}_{23}\text{C}_6$  ( $\text{M} = \text{Fe, Cr, Mo}$ ) phase is consistent with the TEM results. The precipitation temperature of molybdenum carbides is lower than that of chromium carbides. Therefore, molybdenum carbides are first precipitated at about 400°C and converted into  $\text{M}_{23}\text{C}_6$  at 600 - 700°C. The precipitates are composite carbides  $(\text{Fe, Cr, Mo})_{23}\text{C}_6$ . The other crystal phase is considered to be  $\gamma$ -(Fe, Cr, Mo). Fig. 11 shows the EDS analysis results of the two-phase boundary  $\text{M}_{23}\text{C}_6$  and  $\gamma$ -(Fe, Cr, Mo) and the scanning position is shown in Fig. 11(a).

It can be seen that there are more Mo elements in  $\gamma$ -(Fe, Cr, Mo) than in  $M_{23}C_6$ . Although iron and molybdenum have similar binding capabilities with carbon, iron requires less carbon, and  $Fe_{23}C_6$  is more stable than  $Mo_{23}C_6$ . The content of iron in  $M_{23}C_6$  is higher than that of molybdenum. In  $M_{23}C_6$ , since the atomic radius of iron is smaller than that of molybdenum, it does not cause excessive lattice distortion.

Owing to the XRD results, there are only  $M_{23}C_6$  and  $\gamma$ -(Fe,Cr,Mo) in the middle of the coating. Therefore, the white phase at the center of the unit structure and the white needle-like phase at the boundary are the same crystal phase  $\gamma$ -(Fe, Cr, Mo). Due to the low content of the black phase at the boundary of the unit structure, the existence of this phase has not been confirmed in XRD experiments. The results show that the disordered solid solution  $\gamma$ -(Fe, Cr, Mo) phase has formed an ordered solid solution. This is why the  $110$  crystal plane appears in the diffraction pattern of  $\gamma$ -(Fe, Cr, Mo).

For multiphase alloys, the phase boundary is an important factor affecting the material properties [53]. Fig. 10(f) shows the HRTEM image of the edges of the  $\gamma$ -(Fe, Cr, Mo) phase and  $M_{23}C_6$  phase. It can be seen that the  $\gamma$ -(Fe, Cr, Mo) phase and the  $M_{23}C_6$  phase are tightly combined at the edge, and some atomic vacancies or deletions are found. This is because the rapid solidification of laser cladding causes defects in the crystal to increase the error rate during solidification. These defects based on thermodynamic instability can cause alloying elements to precipitate around them, which in turn affects the mechanical properties of the coating. And the boundary exhibits a sawtooth shape, so it can be considered that there is a tighter bond between the two crystal phases.

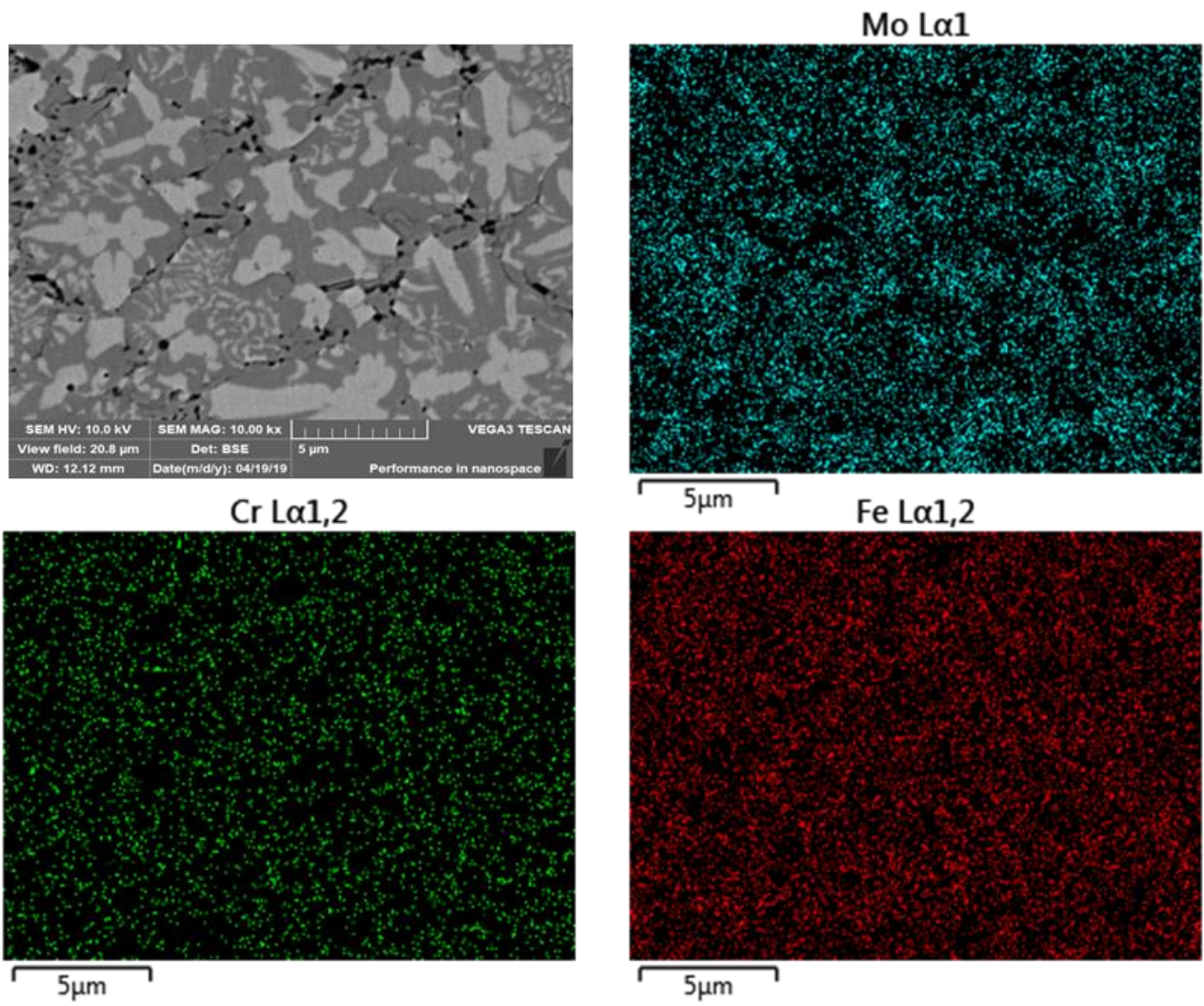
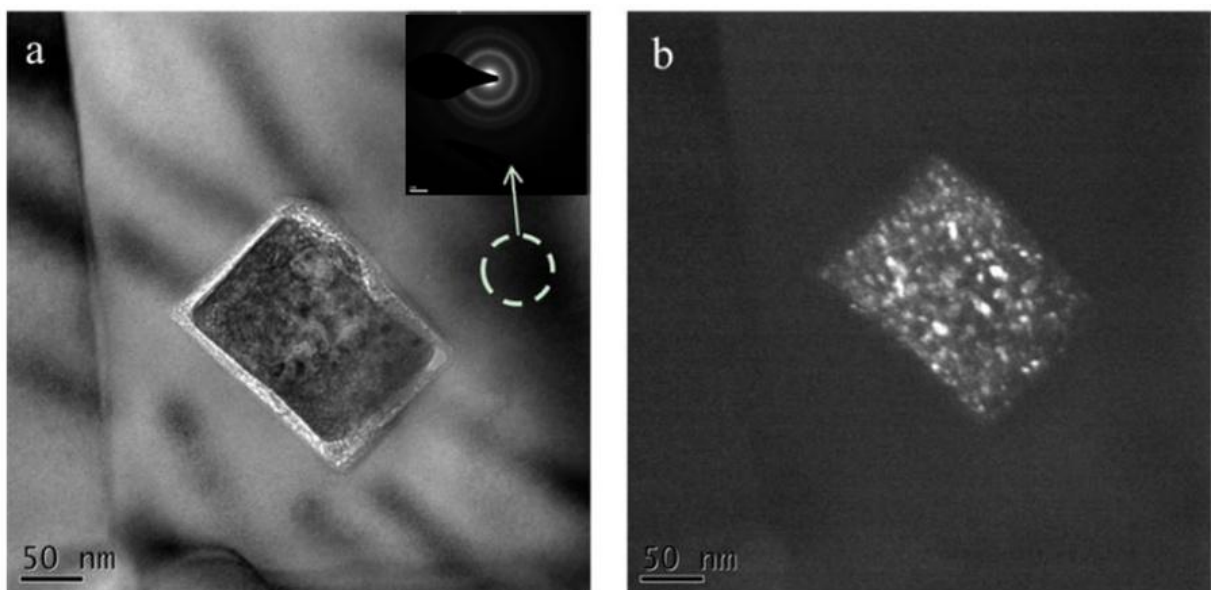
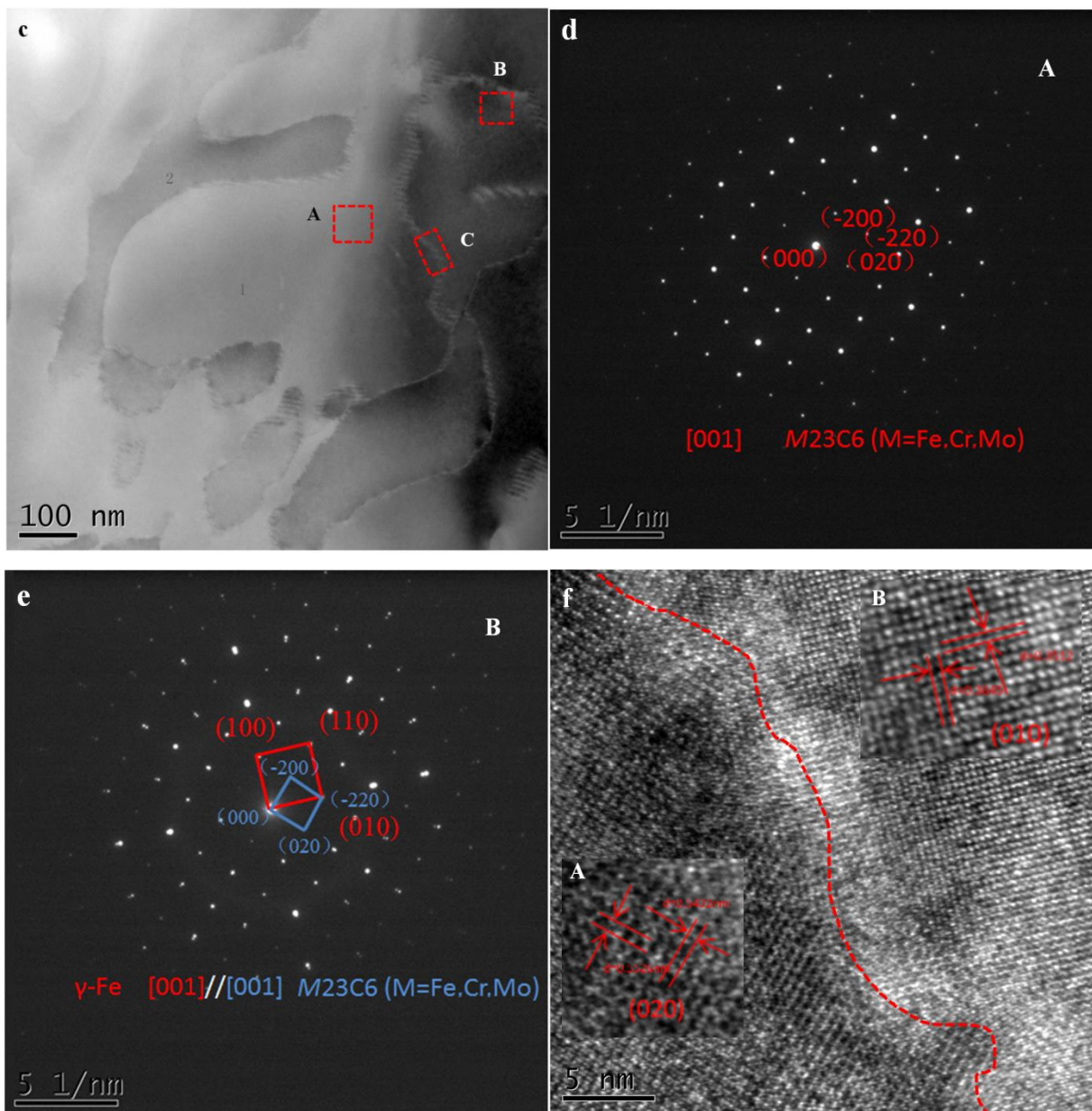


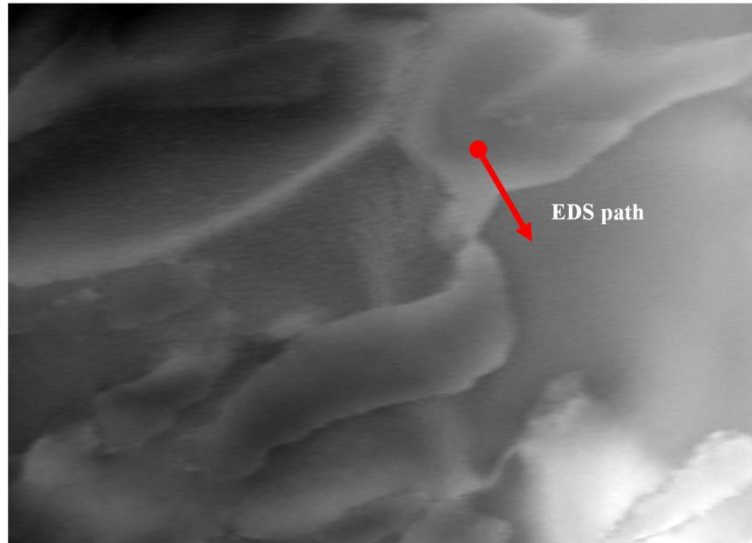
Fig 9 Mapping scanning results of the coating



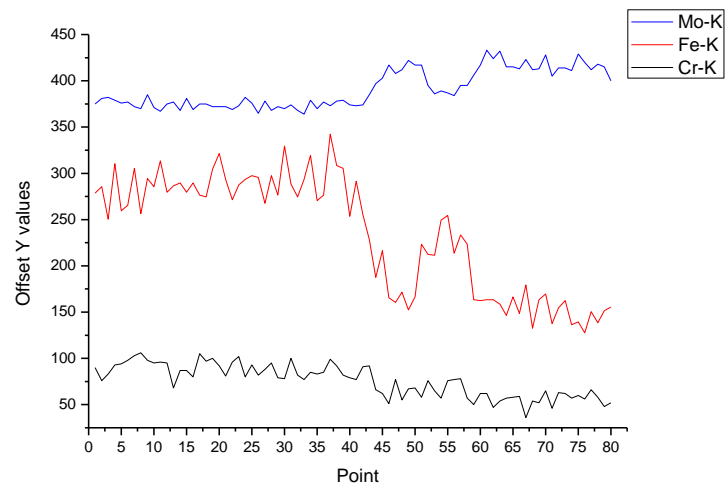


(a) Brightfield image of amorphous phase area; (b) Dark field image of Amorphous phase area; (c) TEM images of composite structures of the coating; (d) Selected area electron diffraction (SAED) of area A in Figure 10 (c); (e) Selected area electron diffraction (SAED) of area B in Figure 10 (c); (f) high resolution transmission electron microscopy (HRTEM) images of area C in Figure 10 (c)

Fig 10 TEM analysis of the coating



(a) The scanning position of EDS test (phases boundary)



(b) EDS result of phases boundary

Fig. 11 EDS spectrum of the two-phase boundary

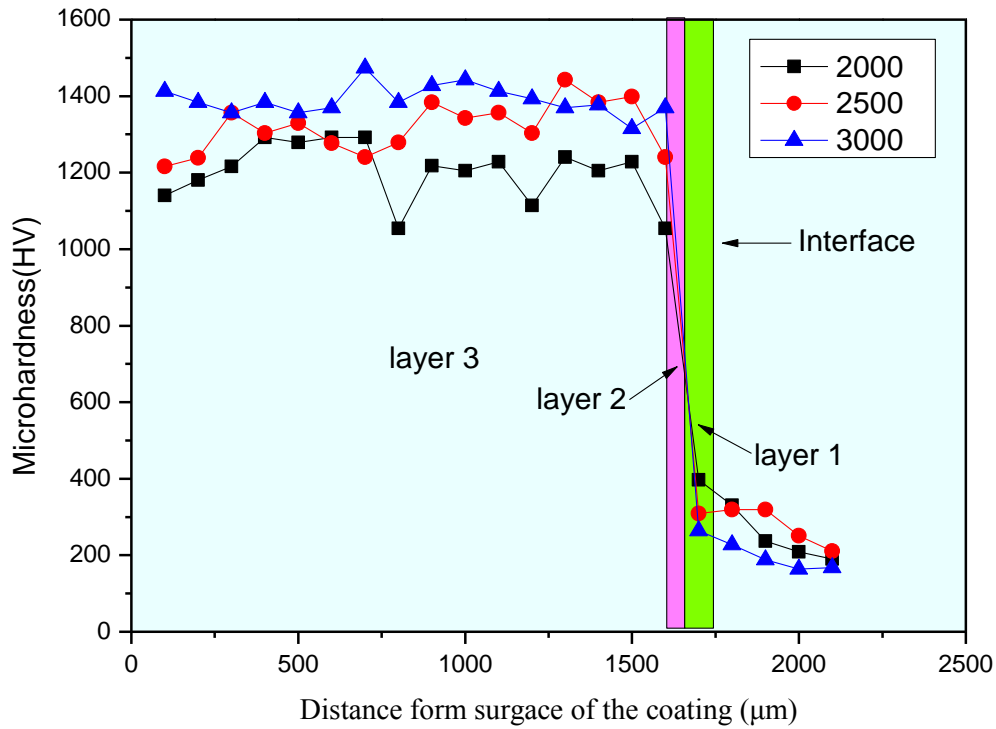


Fig. 12 Micro-hardness distribution along depth direction

#### 4. Wear and nanoindentation test

##### 4.1 Wear test

The microhardness of the three coatings is shown in Fig. 12. It can be clearly found that the hardness distribution curve of each coating has no obvious fluctuations, and the microhardness distribution is basically uniform. That is because the main structure of the coating is similar, and they are all unit structures composed of crystalline phase and amorphous phase. The third layer has the largest microhardness, with a hardness value of 1447.9 HV and an average microhardness of 1353 HV. Due to the presence of the crystalline phase in the second layer, this reduces the microhardness of the coating. And because there are columnar crystals in the first layer, the microhardness of the coating is greatly reduced. The results show that the microhardness of the iron-based amorphous coating prepared by laser cladding technology is much higher than that of the matrix phase. Despite the presence of a crystalline phase, the presence of amorphous increases the microhardness of the third layer.

The depth of the wear trace of the coating is less than that of the substrate, as shown in Fig. 13(d). The depth of the wear trace of the coating is 2.99  $\mu\text{m}$ , and the depth of the wear trace of the base material is 52.31  $\mu\text{m}$ , which is about 20 times the thickness of the coating. At room temperature, due to the positive load and friction acting on the surface of the coating, it is easy to form cracks and expansion on the surface of the coating, with poor fracture

toughness, and even peeling. During the experiment, a part of the coating surface will fall off, as shown in Fig. 13(b). The existence of cracks can be clearly seen in Fig. 13(a). Obviously, there are scratches on the worn surface. Obviously, this is mainly due to the presence of a white crystalline phase in the amorphous layer of this layer. At a large cooling rate, there is not enough time for the white crystalline phase to grow. This does not mean that the bonding ability of the white crystalline phase and the amorphous phase is poor. The white crystalline phase is firmly bonded to the coating, as shown in Fig. 13(a). It can be seen that the white particle phase is significantly higher than the surrounding coating, which proves that it is not only firmly bonded to the substrate, but also has better wear resistance.

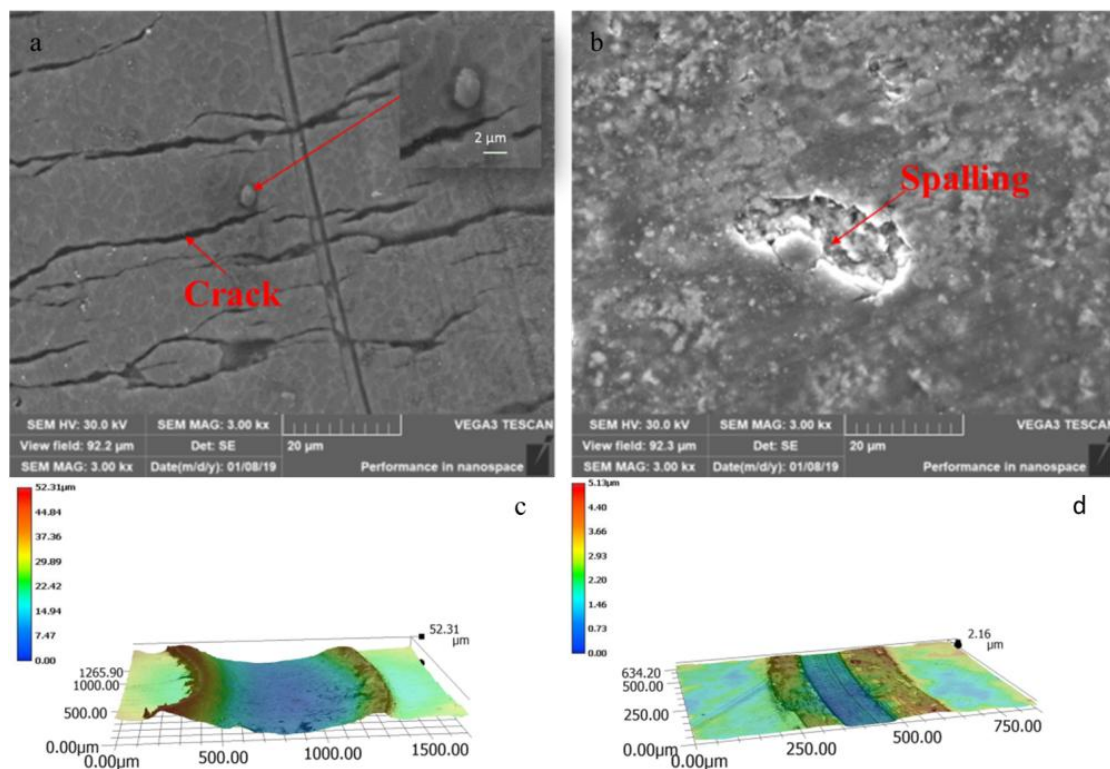


Fig. 13. (a) SEM micrographs showing the worn surface morphologies of coatings (b) Friction coefficient of coatings and base metal (c) 3D map of wear morphology of coating (d) 3D map of wear morphology of substrate

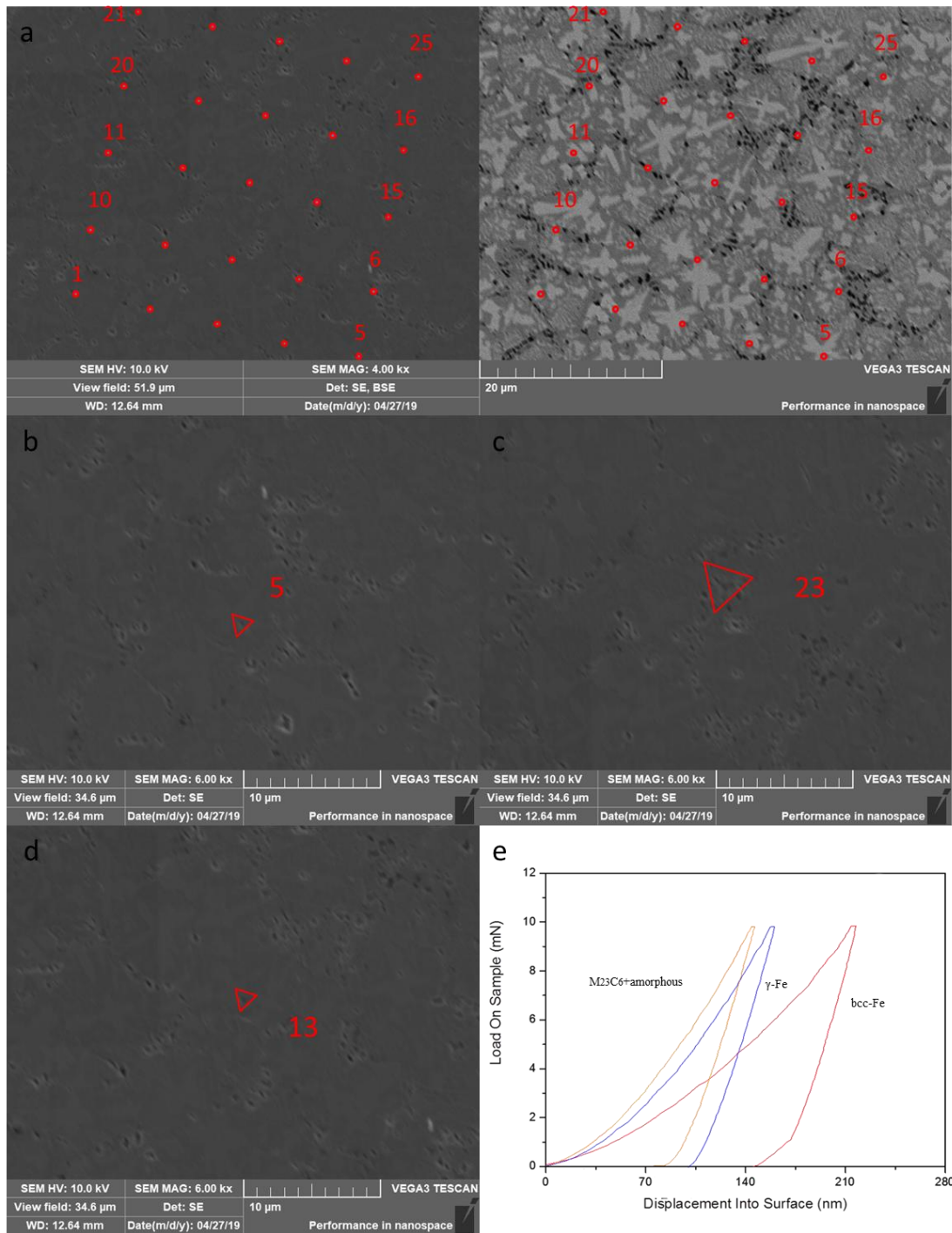


Fig. 14 (a) The matrix of nanoindentation (b) Nanoindentation morphology of  $M_{23}C_6$  (c) Nanoindentation morphology of bcc-Fe (d) Nanoindentation morphology of  $\gamma$ -(Fe, Cr, Mo) (e) load-displacement curves of different regions

#### 4.2 Nanoindentation test

The microhardness cannot accurately determine the mechanical properties of different phases in the amorphous phase region. Therefore, nanoindentation is applied to the amorphous phase region of the coating.

Nanoindentation topography of  $\gamma$ -(Fe, Cr, Mo),  $M_{23}C_6$  and bcc-Fe is shown in the Fig. 14. The area of the indentation area bcc-Fe is larger than that of  $\gamma$ -(Fe,Cr,Mo) and  $M_{23}C_6$ . This demonstrates that the presence of bcc-Fe can effectively increase the plasticity of the coating and reduce the tendency of the amorphous coating to crack due to high brittleness. No cracks appear around the indentation, which proves that the coating has some toughness. And a large number of shear bands are not found at the edge of the indentation, which is determined by the brittleness of the coating itself. The presence of non-metallic elements in the coating results in the presence of ionic bonds which is detrimental to the plastic deformation. When the indentation is driven into the mixed region of amorphous and  $M_{23}C_6$ , since the amorphous is relatively dense, the indentation size at the crystal does not increase infinitely with the depth of the indenter. The figure shows that the load-displacement curves of the white phase  $\gamma$ -(Fe,Cr,Mo),  $M_{23}C_6$  amorphous mixed region and bcc-Fe region in the cladding layer are compared by the maximum displacement of the indentation. The plasticity of the amorphous and  $M_{23}C_6$  mixed regions after the indentation test is found to be less deformation.

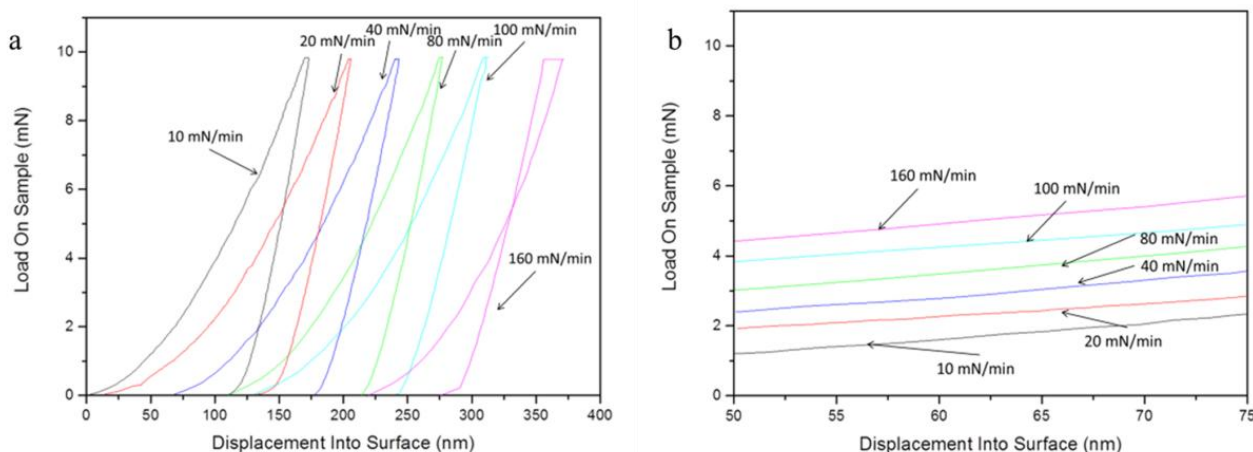


Fig.15 (a) Load-displacement curves at different loading rates (b) Partial enlargement of the curve

In order to better obtain the mechanical properties of the amorphous region, the nanoindentation test was performed on the amorphous regions in the coating by different loading speeds and the results are shown in Fig. 15 (a). It can be seen that the loading curves exhibit an unstable state with increasing loading speed. When the loading speed reaches 100 mN/min, the curve is unstable, and when it reaches 160 mN/min, it shows a complete instability state. On the other hand, when the loading speed is too fast, the plastic deformation has no time to expand, so that the deformation shows a rebound trend, which affects the detection results. Fig. 15(b) shows the results of magnifying the curve loading segment at different loading speeds. It can be seen from the amplification curve that the curve fluctuation is more obvious at lower loading speed. The formation and expansion of the shear band of amorphous alloy during plastic deformation can lead to the occurrence of such fluctuations [54]. During the

pressing of the indenter into the coating, the stress in the local area of the indentation point tends to be concentrated. When the pressure reaches a certain value, the formation and expansion of the shear band occurs. As the release rate of the elastic potential energy is greater than the diffusion speed of the shear band, the discontinuity of the deformation feature is caused, and the load displacement curve fluctuates [55]. However, since the amorphous phase region in the coating is a mixture of amorphous phase and crystalline phase, the fluctuation is not strong enough to exhibit a serrated rule.

## 5. Conclusions

In this study, laser cladding has been proved to be an effective method for preparing Fe-Cr-Mo-C-Y amorphous coating on Q235 steel substrate. Through detailed investigation, the following conclusions can be drawn:

- a. By properly adjusting the laser scanning speed under the condition of a fixed laser power, a laser cladding coating without macroscopic defects can be obtained. The microstructure of the coating can be divided into three layers: the first layer (columnar crystals), the second layer (the crystalline phase filled with the unit structure) and the third layer (the unit structure consists of a crystalline phase and an amorphous phase). X-ray diffraction analysis confirmed the presence of  $M_{23}C_6$  ( $M = Fe, Cr, Mo$ ),  $\gamma$ -(Fe, Cr, Mo) and bcc-Fe. And as the scanning speed increases, the peaks are significantly reduced, while the wider diffraction peaks increase.
- b. The microhardness of the coating is significantly increased to 1447.9 HV. As the crystallization of the coating is more obvious at the bottom, the hardness starts to decrease in the second layer. The introduction of nanoindentation successfully proved the role of different phases in the amorphous phase region. The fluctuation of the curve in the variable load test indirectly proves the presence of an amorphous phase in the layer.
- c. TEM diffraction analysis confirmed that in the unit structure of the third layer, the precipitation phases growing from the edge to the middle are  $\gamma$ -(Fe, Cr, Mo) and  $M_{23}C_6$  ( $M = Fe, Cr, Mo$ ). Compared with the energy spectrum results, it is proved that the white acicular phase and white equiaxed crystal are  $\gamma$ -(Fe, Cr, Mo), and the black acicular phase is  $M_{23}C_6$  ( $M = Fe, Cr, Mo$ ). Combined with the XRD results, it is proved that the amorphous phase is between the needle-like precipitate phase and the equiaxed crystal in the middle of the unit structure.

## Acknowledgements

This research was supported by National Natural Science Foundation of China (52075317, 51805315, 51805316,

51905333), the Royal Society through International Exchanges 2018 Cost Share (China) scheme (IEC\NSFC\181278), Shanghai Sailing Program (19YF1418100), Shanghai Science and Technology Committee Innovation Grant (17JC1400600, 17JC1400601, 19511106400, 19511106402), Karamay Science and Technology Major Project (2018ZD002B), Aid for Xinjiang Science and Technology Project (2019E0235), Shanghai Local Colleges and Universities Capacity Building Special Plan Project (19030501300).

## Reference

- [1] P. Zhang, X. Liu, H. Yan, Phase composition, microstructure evolution and wear behavior of Ni-Mn-Si coatings on copper by laser cladding, *Surf. Coatings Technol.* 332 (2017) 504–510.  
<https://doi.org/10.1016/j.surfcoat.2017.08.072>.
- [2] Q. Zhuang, P. Zhang, M. Li, H. Yan, Z. Yu, Q. Lu, Microstructure, wear resistance and oxidation behavior of Ni-Ti-Si coatings fabricated on Ti6Al4V by laser cladding, *Materials (Basel)*. 10 (2017).  
<https://doi.org/10.3390/ma10111248>.
- [3] P. Niu, R. Li, S. Zhu, M. Wang, C. Chen, T. Yuan, Hot cracking, crystal orientation and compressive strength of an equimolar CoCrFeMnNi high-entropy alloy printed by selective laser melting, *Opt. Laser Technol.* 127 (2020) 106147. <https://doi.org/10.1016/j.optlastec.2020.106147>.
- [4] L. Li, R. Li, T. Yuan, C. Chen, Z. Zhang, X. Li, Microstructures and tensile properties of a selective laser melted Al-Zn-Mg-Cu (Al7075) alloy by Si and Zr microalloying, *Mater. Sci. Eng. A*. 787 (2020) 139492.  
<https://doi.org/https://doi.org/10.1016/j.msea.2020.139492>.
- [5] H. Yan, P. Zhang, Z. Yu, Q. Lu, S. Yang, C. Li, Microstructure and tribological properties of laser-clad Ni-Cr/TiB<sub>2</sub> composite coatings on copper with the addition of CaF<sub>2</sub>, *Surf. Coatings Technol.* 206 (2012) 4046–4053. <https://doi.org/10.1016/j.surfcoat.2012.03.086>.
- [6] H. Yan, P. Zhang, Q. Gao, Y. Qin, R. Li, Laser cladding Ni-based alloy/nano-Ni encapsulated h-BN self-lubricating composite coatings, *Surf. Coatings Technol.* 332 (2017) 422–427.  
<https://doi.org/https://doi.org/10.1016/j.surfcoat.2017.06.079>.
- [7] Z. Peilei, L. Xiaopeng, L. Yunlong, Y. Hua, Y. Zhishui, L. Chonggui, L. Qinghua, Microstructure and wear behavior of Cu-Mo-Si coatings by laser cladding, *Appl. Surf. Sci.* 311 (2014) 709–714.  
<https://doi.org/10.1016/j.apsusc.2014.05.141>.
- [8] J. Cheng, B. Sun, Y. Ge, X. Hu, L. Zhang, X. Liang, X. Zhang, Effect of B/Si ratio on structure and properties of high-entropy glassy Fe<sub>25</sub>Co<sub>25</sub>Ni<sub>25</sub>(B<sub>x</sub>Si<sub>1-x</sub>)<sub>25</sub> coating prepared by laser cladding, *Surf. Coatings Technol.* 402 (2020) 126320. <https://doi.org/https://doi.org/10.1016/j.surfcoat.2020.126320>.

- [9] S. Kaierle, L. Overmeyer, I. Alfred, B. Rottwinkel, J. Hermsdorf, V. Wesling, N. Weidlich, Single-crystal turbine blade tip repair by laser cladding and remelting, *CIRP J. Manuf. Sci. Technol.* 19 (2017) 196–199. <https://doi.org/10.1016/j.cirpj.2017.04.001>.
- [10] S. Guo, H. Shang, L. Cui, X. Guo, J. Yao, Effects of Laser Cladding Layers Width on Total Indicated Runout Characteristics of Steam Turbine Rotor Surface, *Xiyou Jinshu Cailiao Yu Gongcheng/Rare Met. Mater. Eng.* 46 (2017) 612–616. [https://doi.org/10.1016/s1875-5372\(17\)30105-4](https://doi.org/10.1016/s1875-5372(17)30105-4).
- [11] W. Yuan, R. Li, Z. Chen, J. Gu, Y. Tian, A comparative study on microstructure and properties of traditional laser cladding and high-speed laser cladding of Ni45 alloy coatings, *Surf. Coatings Technol.* (2020) 126582. <https://doi.org/10.1016/j.surfcoat.2020.126582>.
- [12] X. Xu, H.F. Lu, K.Y. Luo, J.H. Yao, L.Z. Xu, J.Z. Lu, Y.F. Lu, Mechanical properties and electrochemical corrosion resistance of multilayer laser clad Fe-based composite coatings on 4Cr5MoSiV1 steel, *J. Mater. Process. Technol.* 284 (2020) 116736. <https://doi.org/10.1016/j.jmatprotec.2020.116736>.
- [13] J. Cheng, Y. Feng, C. Yan, X. Hu, R. Li, X. Liang, Development and Characterization of Al-Based Amorphous Coating, *JOM.* 72 (2020) 745–753. <https://doi.org/10.1007/s11837-019-03966-y>.
- [14] P. Zhang, H. Yan, P. Xu, Z. Yu, C. Li, Microstructure and tribological behavior of amorphous and crystalline composite coatings using laser melting, *Appl. Surf. Sci.* 258 (2012) 6902–6908. <https://doi.org/10.1016/j.apsusc.2012.03.130>.
- [15] A. Inoue, F.L. Kong, Q.K. Man, B.L. Shen, R.W. Li, F. Al-Marzouki, Development and applications of Fe- and Co-based bulk glassy alloys and their prospects, *J. Alloys Compd.* 615 (2014) S2–S8. <https://doi.org/10.1016/j.jallcom.2013.11.122>.
- [16] P. Bordeenithikasem, M. Stolpe, A. Elsen, D.C. Hofmann, Glass forming ability, flexural strength, and wear properties of additively manufactured Zr-based bulk metallic glasses produced through laser powder bed fusion, *Addit. Manuf.* 21 (2018) 312–317. <https://doi.org/10.1016/j.addma.2018.03.023>.
- [17] A. Basu, A.N. Samant, S.P. Harimkar, J.D. Majumdar, I. Manna, N.B. Dahotre, Laser surface coating of Fe–Cr–Mo–Y–B–C bulk metallic glass composition on AISI 4140 steel, *Surf. Coatings Technol.* 202 (2008) 2623–2631. <https://doi.org/10.1016/J.SURFCOAT.2007.09.028>.
- [18] I. Manna, J. Dutta Majumdar, B. Ramesh Chandra, S. Nayak, N.B. Dahotre, Laser surface cladding of Fe–B–C, Fe–B–Si and Fe–BC–Si–Al–C on plain carbon steel, *Surf. Coatings Technol.* 201 (2006) 434–440. <https://doi.org/10.1016/J.SURFCOAT.2005.11.138>.
- [19] P. Zhang, H. Yan, C. Yao, Z. Li, Z. Yu, P. Xu, Synthesis of Fe-Ni-B-Si-Nb amorphous and crystalline composite

- coatings by laser cladding and remelting, *Surf. Coatings Technol.* 206 (2011) 1229–1236.  
<https://doi.org/10.1016/j.surfcoat.2011.08.039>.
- [20] T.T. Wong, G.Y. Liang, Formation and Crystallization of Amorphous Structure in the Laser-Cladding Plasma-Sprayed Coating of Al-Si Alloy, *Mater. Charact.* 38 (1997) 85–89.  
[https://doi.org/10.1016/s1044-5803\(97\)80027-7](https://doi.org/10.1016/s1044-5803(97)80027-7).
- [21] L. Zhang, C. Wang, L. Han, C. Dong, Influence of laser power on microstructure and properties of laser clad Co-based amorphous composite coatings, *Surfaces and Interfaces.* 6 (2017) 18–23.  
<https://doi.org/10.1016/j.surfin.2016.11.006>.
- [22] F. Shu, Z. Tian, H. Zhao, W. He, S. Sui, B. Liu, Synthesis of amorphous coating by laser cladding multi-layer Co-based self-fluxed alloy powder, *Mater. Lett.* 176 (2016) 306–309.  
<https://doi.org/10.1016/j.matlet.2016.04.118>.
- [23] M. Aghasibeig, H. Fredriksson, Laser cladding of a featureless iron-based alloy, *Surf. Coatings Technol.* 209 (2012) 32–37. <https://doi.org/10.1016/j.surfcoat.2012.08.013>.
- [24] Q. Zhang, P. Zhang, H. Yan, Z. Yu, D. Wu, H. Shi, S. Li, Y. Tian, Magnetic-field-assisted laser cladding in the preparation of a crack-free Fe-Cr-Mo-C-Y-B amorphous coating on steel, *Philos. Mag. Lett.* 100 (2020) 86–93.  
<https://doi.org/10.1080/09500839.2020.1725245>.
- [25] R. Li, Z. Li, J. Huang, P. Zhang, Y. Zhu, Effect of Ni-to-Fe ratio on structure and properties of Ni-Fe-B-Si-Nb coatings fabricated by laser processing, *Appl. Surf. Sci.* 257 (2011) 3554–3557.  
<https://doi.org/10.1016/j.apsusc.2010.11.073>.
- [26] P. Zhang, H. Yan, P. Xu, Q. Lu, C. Li, Z. Yu, Influence of different annealing temperatures and cooling rates on amorphous and crystalline composite coating, *Surf. Coatings Technol.* 206 (2012) 4981–4987.  
<https://doi.org/10.1016/j.surfcoat.2012.05.142>.
- [27] Z. Peilei, L. Yunlong, Y. Hua, M. Kai, X. Peiquan, Y. Zhishui, C. Yingying, D. Min, Effect of Nb addition on Fe-Ni-B-Si amorphous and crystalline composite coatings by laser processing, *Surf. Coatings Technol.* 236 (2013) 84–90. <https://doi.org/10.1016/j.surfcoat.2013.09.032>.
- [28] A. Inoue, A. Takeuchi, Recent progress in bulk glassy, nanoquasicrystalline and nanocrystalline alloys, *Mater. Sci. Eng. A.* (2004). <https://doi.org/10.1016/j.msea.2003.10.159>.
- [29] S.L. Wang, Z.Y. Zhang, Y.B. Gong, G.M. Nie, Microstructures and corrosion resistance of Fe-based amorphous/nanocrystalline coating fabricated by laser cladding, *J. Alloys Compd.* 728 (2017) 1116–1123.  
<https://doi.org/10.1016/j.jallcom.2017.08.251>.

- [30] H. Sahasrabudhe, A. Bandyopadhyay, Laser processing of Fe based bulk amorphous alloy coating on zirconium, *Surf. Coatings Technol.* 240 (2014) 286–292. <https://doi.org/10.1016/J.SURFCOAT.2013.12.043>.
- [31] R. Li, Z. Li, J. Huang, Y. Zhu, Dilution effect on the formation of amorphous phase in the laser clad Ni-Fe-B-Si-Nb coatings after laser remelting process, *Appl. Surf. Sci.* 258 (2012) 7956–7961. <https://doi.org/10.1016/j.apsusc.2012.04.144>.
- [32] W. Xing, D. Ouyang, N. Li, L. Liu, Insight into micro-cracking in 3D-printed Fe-based BMGs by selective laser melting, *Intermetallics*. 103 (2018) 101–106. <https://doi.org/10.1016/j.intermet.2018.10.011>.
- [33] P. Zhang, D. Ouyang, L. Liu, Enhanced mechanical properties of 3D printed Zr-based BMG composite reinforced with Ta precipitates, *J. Alloys Compd.* 803 (2019) 476–483. <https://doi.org/10.1016/j.jallcom.2019.06.303>.
- [34] Y.M. Zou, Y.S. Wu, K.F. Li, C.L. Tan, Z.G. Qiu, D.C. Zeng, Selective laser melting of crack-free Fe-based bulk metallic glass via chessboard scanning strategy, *Mater. Lett.* 272 (2020) 2–5. <https://doi.org/10.1016/j.matlet.2020.127824>.
- [35] X. Cheng, S. Liu, C. Chen, W. Chen, M. Liu, R. Li, X. Zhang, K. Zhou, Microstructure and mechanical properties of additive manufactured porous Ti–33Nb–4Sn scaffolds for orthopaedic applications, *J. Mater. Sci. Mater. Med.* 30 (2019) 91. <https://doi.org/10.1007/s10856-019-6292-0>.
- [36] D. Yang, H. Li, S. Liu, C. Song, Y. Yang, S. Shen, J. Lu, Z. Liu, Y. Zhu, In situ capture of spatter signature of SLM process using maximum entropy double threshold image processing method based on genetic algorithm, *Opt. Laser Technol.* 131 (2020) 106371. <https://doi.org/10.1016/j.optlastec.2020.106371>.
- [37] M.L. Montero-Sistiaga, M. Godino-Martinez, K. Boschmans, J.P. Kruth, J. Van Humbeeck, K. Vanmeensel, Microstructure evolution of 316L produced by HP-SLM (high power selective laser melting), *Addit. Manuf.* 23 (2018) 402–410. <https://doi.org/10.1016/j.addma.2018.08.028>.
- [38] A. Langlet, US8052923B2-Method of producing products of amorphous metal- Google Patents, 2 (2011). <https://patents.google.com/patent/US8052923> (accessed November 8, 2011).
- [39] A. Langlet, US8052923B3-Method of producing objects containing nano metal or composite metal-Google Patents, (2011). <https://patents.google.com/patent/US8333922> (accessed November 8, 2011).
- [40] S. Pauly, L. Löber, R. Petters, M. Stoica, S. Scudino, U. Kühn, J. Eckert, Processing metallic glasses by selective laser melting, *Mater. Today*. 16 (2013) 37–41. <https://doi.org/10.1016/j.mattod.2013.01.018>.
- [41] K.F. Kobayashi, Chapter 5 Laser processing, in: C.B.T.-P.M.S. Suryanarayana (Ed.), *Non-Equilibrium Process. Mater.*, Pergamon, 1999: pp. 89–118. [https://doi.org/https://doi.org/10.1016/S1470-1804\(99\)80051-0](https://doi.org/https://doi.org/10.1016/S1470-1804(99)80051-0).

- [42] P. Zhang, H. Yan, P. Xu, Q. Lu, C. Li, Z. Yu, Influence of different annealing temperatures and cooling rates on amorphous and crystalline composite coating, *Surf. Coatings Technol.* 206 (2012) 4981–4987.  
<https://doi.org/10.1016/j.surfcoat.2012.05.142>.
- [43] T.M. Yue, Y.P. Su, Laser cladding of SiC reinforced Zr 65 Al 7.5 Ni 10 Cu 17.5 amorphous coating on magnesium substrate, *Appl. Surf. Sci.* 255 (2008) 1692–1698. <https://doi.org/10.1016/j.apsusc.2008.06.036>.
- [44] G. Muvvala, S. Mullick, A.K. Nath, Development of process maps based on molten pool thermal history during laser cladding of Inconel 718/TiC metal matrix composite coatings, *Surf. Coatings Technol.* 399 (2020) 126100.  
<https://doi.org/10.1016/j.surfcoat.2020.126100>.
- [45] Y.Y. Zhu, Z.G. Li, R.F. Li, M. Li, K. Feng, Y.X. Wu, T. Wada, H. Kato, High power diode laser cladding of Fe-Co-B-Si-C-Nb amorphous coating: Layered microstructure and properties, *Surf. Coatings Technol.* 235 (2013) 699–705. <https://doi.org/10.1016/j.surfcoat.2013.08.050>.
- [46] H. zheng Wang, Y. hai Cheng, X. cheng Zhang, J. yong Yang, C. ming Cao, Effect of laser scanning speed on microstructure and properties of Fe based amorphous/ nanocrystalline cladding coatings, *Mater. Chem. Phys.* 250 (2020) 123091. <https://doi.org/10.1016/j.matchemphys.2020.123091>.
- [47] X. Dai, S. Zhou, M. Wang, J. Lei, C. Wang, T. Wang, Microstructure evolution of phase separated Fe-Cu-Cr-C composite coatings by laser induction hybrid cladding, *Surf. Coatings Technol.* 324 (2017) 518–525.  
<https://doi.org/10.1016/j.surfcoat.2017.06.032>.
- [48] M. Gäumann, S. Henry, F. Cléton, J.D. Wagnière, W. Kurz, Epitaxial laser metal forming: Analysis of microstructure formation, *Mater. Sci. Eng. A.* 271 (1999) 232–241.  
[https://doi.org/10.1016/s0921-5093\(99\)00202-6](https://doi.org/10.1016/s0921-5093(99)00202-6).
- [49] K. Ferjančič, M. Može, P. Križan, M. Bobič, I. Golobič, Subcooled critical heat flux on laser-textured stainless-steel ribbon heaters in pool boiling of FC-72, *Int. J. Heat Mass Transf.* 159 (2020) 120090.  
<https://doi.org/10.1016/j.ijheatmasstransfer.2020.120090>.
- [50] J. Kim, K. Kang, S. Yoon, C. Lee, Enhancement of metallic glass properties of Cu-based BMG coating by shroud plasma spraying, *Surf. Coatings Technol.* 205 (2011) 3020–3026.  
<https://doi.org/10.1016/j.surfcoat.2010.11.012>.
- [51] M. Hillert, C. Qiu, A reassessment of the Fe-Cr-Mo-C system, *J. Phase Equilibria.* 13 (1992) 512–521.  
<https://doi.org/10.1007/BF02665764>.
- [52] S. Xiang, S. Mao, Z. Shen, H. Long, H. Wei, S. Ma, J.X. Zhang, Y. Chen, J. Zhang, B. Zhang, Y. Liu, Site preference of metallic elements in M<sub>23</sub>C<sub>6</sub> carbide in a Ni-based single crystal superalloy, *Mater. Des.* 129 (2017)

9–14. <https://doi.org/10.1016/j.matdes.2017.05.023>.

- [53] G. Qian, Z. Jian, X. Pan, F. Berto, In-situ investigation on fatigue behaviors of Ti-6Al-4V manufactured by selective laser melting, *Int. J. Fatigue*. 133 (2020) 105424.

<https://doi.org/https://doi.org/10.1016/j.ijfatigue.2019.105424>.

- [54] C.A. Schuh, T.G. Nieh, A nanoindentation study of serrated flow in bulk metallic glasses, *Acta Mater.* 51 (2003) 87–99. [https://doi.org/10.1016/S1359-6454\(02\)00303-8](https://doi.org/10.1016/S1359-6454(02)00303-8).

- [55] B.C. Wei, T.H. Zhang, W.H. Li, Y.F. Sun, Y. Yu, Y.R. Wang, Serrated plastic flow during nanoindentation in Nd-based bulk metallic glasses, in: *Intermetallics*, Elsevier, 2004: pp. 1239–1243.

<https://doi.org/10.1016/j.intermet.2004.04.030>.